

Received July 15, 2020, accepted July 23, 2020, date of publication July 27, 2020, date of current version August 7, 2020.

Digital Object Identifier 10.1109/ACCESS.2020.3012133

Solar-Powered Active Integrated Antennas Backed by a Transparent Reflectarray for CubeSat Applications

YEN-SHENG CHEN^{ID}, (Member, IEEE), YU-HONG WU, AND CHIA-CHI CHUNG

Department of Electronics Engineering, National Taipei University of Technology, Taipei 10608, Taiwan

Corresponding author: Yen-Sheng Chen (yschen@ntut.edu.tw)

This work was supported in part by the National Taipei University of Technology, Taiwan, under Contract NTUT-SZU-109-08, and in part by the Ministry of Science and Technology, Taiwan, under Contract MOST 109-2636-E-027-004.

ABSTRACT A gain-enhancement scheme that combines an active integrated antenna (AIA) and an optically transparent reflectarray on solar cells is proposed for CubeSat applications. As CubeSat antennas require a compact footprint, improving the gain over limited design space is challenging. The proposed gain-enhancement scheme exploits the distinct environmental feature of the space, namely, unlimited and sustainable solar energy. This energy is fed into a microwave power amplifier, which is cascaded with a quasi-Yagi antenna. This AIA approach can increase the gain by 22.7 dB. Furthermore, the AIA is arranged as the feed of the transparent reflectarray, which provides twofold advantages. First, the gain can be further improved by 11.0 dB; second, this transparent reflectarray is placed on already existing solar panels, so no additional clearance area is required. We organize the proposed scheme by three modules, including an AIA module, a reflectarray module, and a power management module. The proposed scheme is demonstrated by a prototype designed at 25.0 GHz. By fabricating the transparent reflectarray using Indium Tin Oxide printed on soda-lime glass, the proposed antenna provides realized gain of 41.3 dB with dimensions of $110 \times 80 \text{ mm}^2$; meanwhile, onboard electronics can still be activated due to the power management.

INDEX TERMS Directive antennas, microwave amplifiers, satellite antennas, transmitting antennas.

I. INTRODUCTION

The gain enhancement of antennas has gathered great importance in radiofrequency (RF) satellite communications. As long-distance transmission is required for this application, severe path loss occurs and decreases receiving signal strengths. This limitation can be mitigated using high-gain antennas. Conventional, large satellites that weigh greater than 500 kg have little difficulty in employing a high-gain antenna. The design space of the antenna is large and sufficient, so electrically-large high-gain antennas, such as reflector antennas [1], can be directly mounted to provide precise satellite pointing.

Recently, smallSats that weigh below 500 kg are getting considerable attentions in space industries [2]. In particular, pico-satellites (0.1–1.0 kg) or CubeSats (< 1.33 kg) have increasingly been the object of study due to the

cost-efficient characteristic. For CubeSats applications, high-gain antenna development becomes challenging. The gain enhancement usually requires larger design space, but the limited volume available onboard CubeSats makes performance optimization difficult. Several antenna structures that address high-gain features have been proposed, including reflectors [3], [4], lens [5], reflectarrays [6], leaky-wave antennas [7], slots [8], spirals [9], [10], patches [11]–[18], and patch arrays [19]–[22]. The gain, design volumes, operating frequencies of these antennas are provided in Table 1.

In Table 1, the highest gain, namely, 42.0 dBi, is attained using a mesh reflector antenna designed at 35.75 GHz [4]. The diameter of the reflector is 500 mm. In addition, an inflatable antenna is proposed to depict peak gain of 32.8 dBi at X band [3]. The diameter of the inflatable reflector is 713 mm. Most of the antennas depict peak gain of about 10 dBi [8]–[22] below 10 GHz. These antennas are implemented on a planar area, instead of pursuing a deployable design. However, two limitations are observed. First, these

The associate editor coordinating the review of this manuscript and approving it for publication was Jenny Mahoney.

TABLE 1. Performance comparison for CubeSat antennas.

No.	Antenna Structure	Frequency band	Size ($\lambda \times \lambda$)	Gain (dB)
[3]	Reflector	X band	18.8 × 18.8	32.8
[4]	Reflector	Ka band	59.6 × 59.6	42.0
[5]	Lens	Ka band	8.6 × 7.8	23.3
[6]	Reflectarray	X band	16.8 × 9.4	26.2
[7]	Bull's Eye	V band	20.0 × 20.0	15.4
[8]	Slot array	S band	1.8 × 1.8	10.0
[9]	Conical spiral	S band	0.8 × 0.8	8.4
[10]	Spiral	UHF	1.3 × 1.3	5.6
[11]	Patch	S band	0.8 × 0.8	6.0
[12]	Patch	S band	0.6 × 0.6	7.3
[13]	Patch	S band	0.9 × 1.1	12.0
[14]	Patch	S band	0.6 × 0.6	10.1
[15]	Patch	L band	0.6 × 0.6	5.4
[16]	Patch	S band	0.7 × 0.7	3.5
[17]	Patch	S band	0.8 × 0.8	3.7
[18]	Patch	S band	0.8 × 0.8	7.3
[19]	Patch array	S band	5.2 × 3.0	6.5
[20]	Patch array	X band	3.3 × 3.3	14.7
[21]	Patch array	S band	0.8 × 0.8	4.8
[22]	Patch array	S band	0.8 × 0.8	9.6
This study	AIA with a reflectarray	K band	9.2 × 6.7	41.3

gain-enhancement techniques are based on conventional structures for microwave communications. We lack a design that aims at the environmental feature of the space, which is full of unlimited and sustainable solar energy. Second, although several high-gain antennas have been proposed, the gain obtained over limited design space still needs to be improved.

In this paper, a gain-enhancement antenna with a compact footprint is proposed for CubeSat applications. The gain enhancement is obtained using an active integrated antenna (AIA) biased by harvested solar energy, and the AIA is further arranged as the feed of a transparent reflectarray on solar panels. Three mechanisms are implemented to improve the antenna gain over limited design space. First of all, CubeSats have been equipped with solar panels, but the harvested solar energy is exploited only for powering onboard electronics. As such solar energy is inexhaustible in the space, we cascade the CubeSat antenna with an additional microwave power amplifier (PA), biasing this PA using the parallelly extracted solar power. This leads to a PA-type AIA [23]–[25], and the peak gain soars by 22.7 dB accordingly. Second, the AIA is further arranged as the feed of the transparent reflectarray, which is fabricated using Indium Tin Oxide (ITO) printed on soda-lime glass. By tailoring the

TABLE 2. Comparison for optically transparent reflectarrays.

No.	Frequency band	Dielectric	Conductor	Size ($\lambda \times \lambda$)	Gain (dB)
[26]	Ka band	Quartz	ITO	6.6 × 6.6	22.2
[27]	X band	AF32	Copper	5.7 × 8.5	23.7
[28]	X band	AF32	Copper	8.5 × 8.5	25.7
[29]	X band	Acrylic	Aluminum	10.9 × 10.9	26.2
[30]	Ka band	Acrylic	Aluminum	15.2 × 15.2	28.7
[31]	Ka band	Soda lime glass	Epitaxial	10.6 × 10.6	27.3
[32]	X band	DRA/SC	Copper	11.4 × 11.4	27.2
[33]	Ka band	Quartz	ITO	4.0 × 4.0	17.1
[34]	X band	AF32	Copper	N/A	23.8
[35]	THz	Quartz	ITO	N/A	33.7
This study	K band	Soda lime glass	ITO	9.2 × 6.7	41.3

geometry of the reflectarray, the gain can be further increased by 11.0 dB. Third, as the reflectarray is optically transparent, it is directly placed on the solar panels. The solar energy can still be mostly harvested, yet no extra clearance area is required for implementing this mechanism. The three features result in an antenna with high gain (41.3 dB) and compact size ($9.2 \times 6.7 \lambda^2$, where λ is the wavelength of a design frequency) for CubeSat applications.

In particular, the design of optically transparent reflectarrays has been discussed in the literature [26]–[35]. The material properties, operating frequencies, dimensions, and gain of these transparent reflectarray antennas are summarized in Table 2. Although several earlier studies have investigated transparent reflectarrays fabricated on solar cells, these studies have not exploited the solar energy to construct a self-biased AIA, which is further integrated with the transparent reflectarray to achieve high gain with compact size.

In what follows, the system setup of the proposed antenna is elaborated first. Each module, including a self-biased PA-type AIA module, an optically transparent reflectarray module, and a dc power management module, is described in detail. Furthermore, a prototype is tested to prove the concept. Finally, the optimized performances supplemented with simulated and measured results are compared with the state-of-the-art.

II. PROPOSED ANTENNA SUB-SYSTEM

The proposed antenna is a sub-system, which is comprised of the three modules. Figure 1 illustrates the schematic of the proposed antenna sub-system. The antenna is cascaded with the amplifier, constructed into a PA-type AIA. The AIA is further employed as the feed of the transparent reflectarray. Meanwhile, the transparent reflectarray covers already existing solar cell panels on the surface of a CubeSat. These solar cells employ a conventional power conversion scheme, whereas the output terminals are divided and parallelly connected to two networks, including onboard electronics and

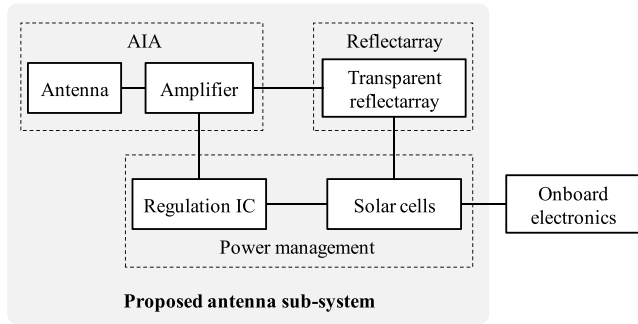


FIGURE 1. Block diagram of the proposed antenna sub-system.

the input of a regulated microchip. The regulated microchip is readily interconnected with the PA. Thus, the uninterrupted solar energy serves the PA as a power supply. Integrating the three modules establishes a simple, self-biased antenna sub-system. This concept is validated by a prototype designed and fabricated at 25.0 GHz.

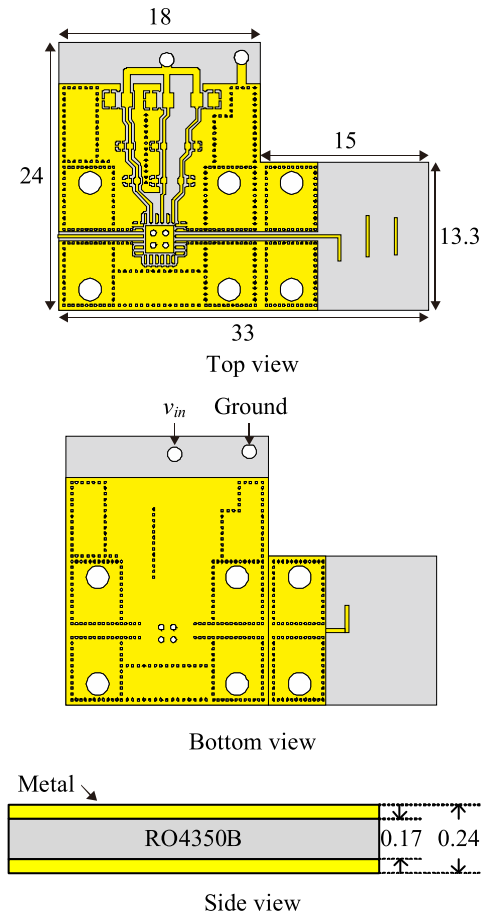


FIGURE 2. Geometry of the AIA module (unit: mm).

A. PA-TYPE AIA

The first module is the PA-type AIA, the geometry of which is shown in Figure 2. The AIA comprises an antenna section and an amplifier section, which are integrated on one printed circuit board (PCB). The substrate used is Rogers

RO4350B (dielectric constant $\epsilon_r = 3.48$ and loss tangent $\tan\delta = 0.0037$). The antenna section is a quasi-Yagi antenna fed by a coplanar waveguide (CPW) transmission line, and the amplifier section consists of an amplifier housed in a leadless ceramic surface mount package and several bypass capacitors.

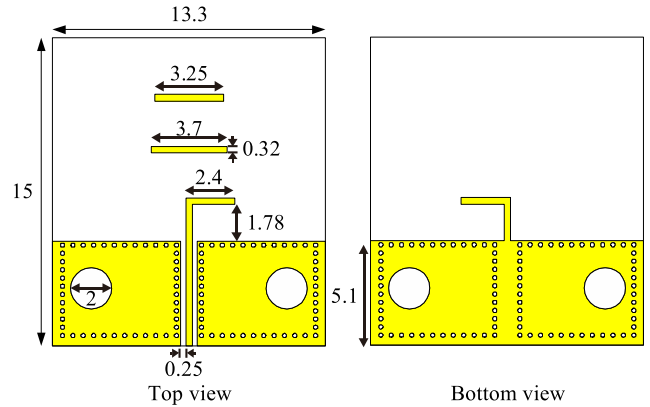


FIGURE 3. Geometry of the quasi-Yagi antenna (unit: mm).

Figure 3 shows the dimensions of the quasi-Yagi antenna. This antenna consists of a driven dipole, two directors, and a ground plane serving as a reflector. The length of the driven dipole is about half-wavelength. The use of CPW feeding can avoid complicated balun design [36]. The reason that we select the quasi-Yagi antenna is its unidirectional and end-fire radiation pattern. When the quasi-Yagi antenna serves a reflectarray as the feed, the blockage effect can be reduced.

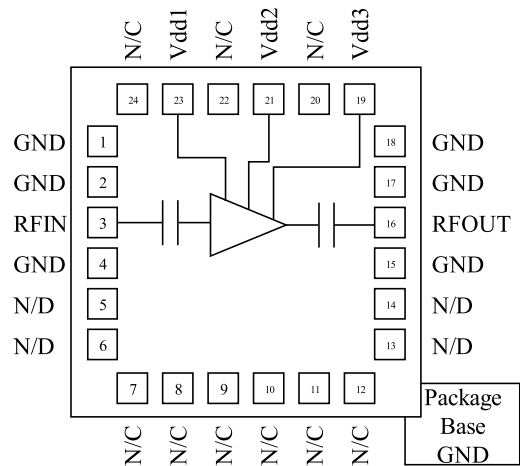


FIGURE 4. Configuration of the MMIC amplifier HMC963LC4.

The PA demonstrated in this study is a self-biased GaAs monolithic microwave integrated circuit (MMIC) low noise amplifier HMC963LC4 from Analog Devices, Norwood, MA. This amplifier operates at 6.0–26.5 GHz, providing small signal gain of 22 dB [37]. Figure 4 provides the functional diagram of this IC. Pins 3 and 16 are the input and output of the signal, respectively, and they are matched to two CPW transmission lines. Pins 19, 21, and 23 are connected to the power management module, and they supply power

collected from solar energy to bias this IC. Three bypass capacitors are used in each bias network. The three bias networks are further combined in parallel, and an input voltage of 3.5 V (denoted by v_{in}) is applied. The associated current is 45 mA, corresponding to a driving power of 157.5 mW. Additionally, pins 1, 2, 4, 15, 17, and 18 are connected to the ground. To ensure the equal reference voltage of the ground, a sufficient number of via holes are mounted to connect the top and bottom ground planes.

The quasi-Yagi antenna and the amplifier are interconnected by CPWs with a characteristic impedance of 50 Ω . As both sections are designed using CPW, the additional loss due to discontinuity as well as the size of the structure can be reduced. This AIA illuminates vertically-polarized wave to the reflectarray surface.

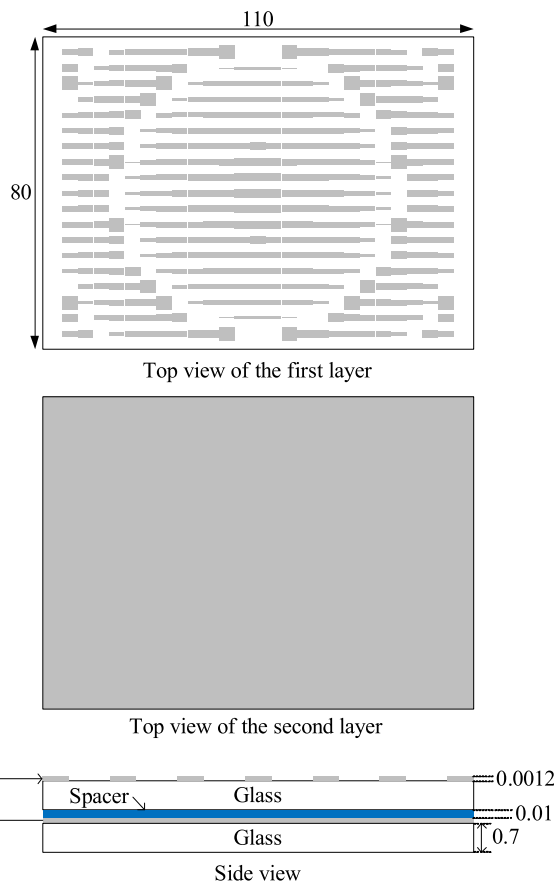


FIGURE 5. Geometry of the transparent reflectarray (unit: mm).

B. OPTICALLY TRANSPARENT REFLECTARRAY

The second module is the optically transparent reflectarray, the geometry of which is shown in Figure 5. The unit cell consists of two layers, which are separated by a 0.01-mm-thick air spacer. The substrate used is soda-lime glass ($\epsilon_r = 7.2$ and $\tan\delta = 0.02$), the thickness of which is 0.7 mm. The transparent conductive material is ITO (conductivity $\sigma = 2.4 \times 10^5$ S/m) made with a 1.2- μm deposition.

A square unit cell with a periodicity of 4.0 mm is implemented. The topology of the unit cell is a rectangular patch

backed with a conductor. As the incidence of the electromagnetic (EM) wave is vertically-polarized, the width of the patch is fixed at 3.1 mm. The length of the patch, which controls the phase of the scattered field, is varied from 0.69 to 3.75 mm. By computing the required phase compensation of each unit cell, the geometry of the full reflectarray can be determined. The number of elements is originally set to $25 \times 25 = 625$; however, as will be detailed in Section III-B, varying the length of the patch cannot offer full 360° phase coverage, so some elements are removed to avoid potential phase errors. This leads to a 423-element transparent reflectarray with dimensions of 110×80 mm² and a focal distance of 80.2 mm.

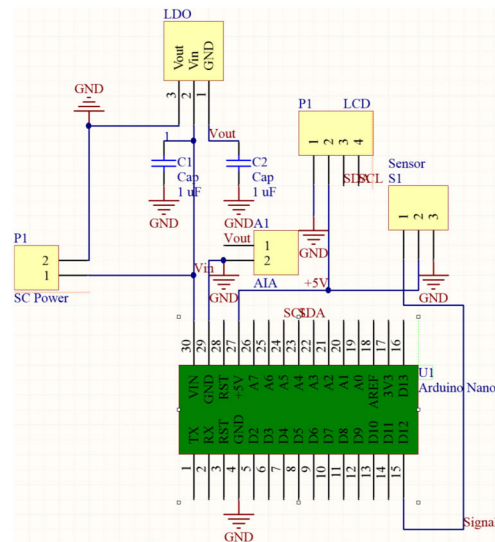


FIGURE 6. Equivalent circuit of the power management module.

C. POWER MANAGEMENT MODULE

The third module is the power management module, aiming at a sustainable and self-biased power supply. Figure 6 shows the equivalent circuit of the power management module designed and simulated using Altium Designer software. After the solar power is converted to dc outputs, this output current is divided up through two parallel networks, namely, a regulated circuit and the input port of onboard electronics.

The regulated microchip is requested for the dc bias to the PA. As the maximum allowable voltage for the PA is 3.5 V, a regulated IC XC6203p352FR-G from Mouser Electronics, Taiwan, is employed to regulate the voltage to $v_{in} = 3.5$ V.

In our prototype, the onboard electronic is implemented as a humidity and temperature sensor DHT11 from Mouser Electronics, Taiwan. The turn-on voltage of DHT11 is 3.0–5.5 V, which is associated with a current of 0.5–2.5 mA. Thus, the maximum driving power of DHT11 is 13.75 mW. This sensor is further integrated to a microprocessor NANO Atmega328p from Arduino, Taiwan. The selected microprocessor is already equipped with an internal voltage regulator, so the signal collected by the sensor can be outputted to

a liquid-crystal display (LCD) without connecting another regulated IC.

III. ANTENNA DESIGN AND PERFORMANCE

The proposed antenna prototype is analyzed and tested. The design process and performance evaluation in terms of each module and the overall system are presented in this section. The experiment on the prototype is conducted in free space, instead of a CubeSat phantom. We fabricate testing fixtures for the feeding antenna and the reflectarray, integrating the three units as a system. Accordingly, the impedance characteristics are tested from the input port of the AIA. Once the feeding quasi-Yagi antenna is excited, the transparent reflectarray creates in-phase reflected wave so that the antenna gain is enhanced. Although the CubeSat phantom is not implemented, testing CubeSat antennas in free space is widely used in the literature [3], [5], [9]–[11], [13]–[16], [18]–[22]. Besides, as the transparent reflectarray is placed above solar panels, the loading effect from onboard electronics can be shielded by the back conductor and the solar cells.

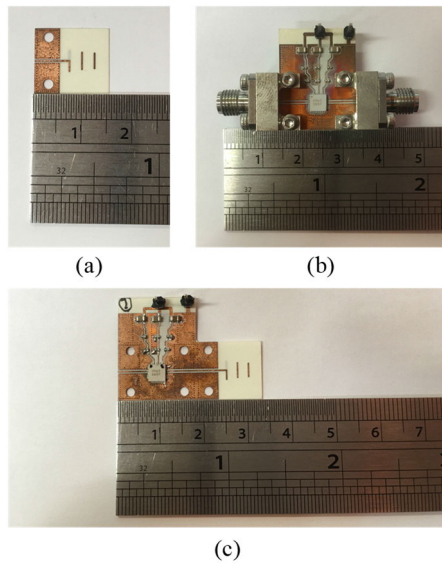


FIGURE 7. Photographs of the AIA module. (a) Quasi-Yagi antenna. (b) Power amplifier network. (c) Active integrated antenna.

A. PA-TYPE AIA

Figure 7 shows photographs of the test pieces for the first module—the PA-type AIA. The quasi-Yagi antenna is designed using CST Microwave Studio, and the circuit regarding the PA is designed using ADS simulation. After the performances of the two sections are evaluated separately, the finalized AIA system is simulated in CST Design Studio, where the two-port scattering parameters of the PA (defined by an s2p file) are loaded into the input of the quasi-Yagi antenna. Thus, this research methodology enables us to test both microwave circuit and full-wave simulation together.

Before providing the overall radiation performances of the AIA, we test the quasi-Yagi antenna and the PA respectively. The impedance matching of the quasi-Yagi antenna is shown

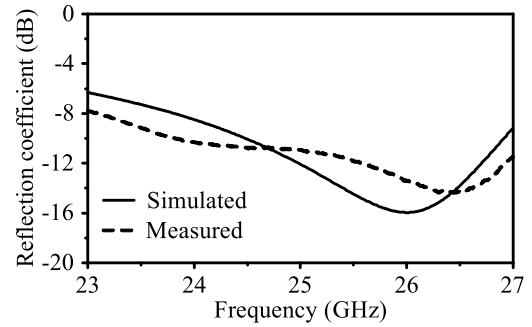


FIGURE 8. Reflection coefficients of the quasi-Yagi antenna.

in Figure 8. At the design frequency (25.0 GHz), the simulated and measured reflection coefficients are -12.1 dB and -10.9 dB, respectively, which indicate that 93.8% and 91.9% of the input power can be accepted by the antenna. The reflection coefficients are evaluated from the antenna looking into a vector network analyzer (VNA). The impedance bandwidth in terms of 10-dB return loss is 10.2% (24.2–26.8 GHz), indicating sufficient impedance matching.

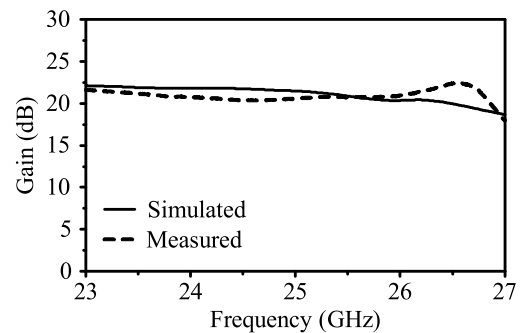


FIGURE 9. Transducer power gain of the power amplifier network.

The design specifications of microwave amplifiers concern the gain, stability, and noise figure. The transducer power gain of the amplifier network is depicted in Figure 9. This transducer gain evaluates the gain of the MMIC amplifier HMC963LC4, the loss of the CPW transmission lines, and the mismatch between the transmission lines and SMA connectors. The simulated and measured transducer power gain at 25.0 GHz are 21.5 dB and 20.6 dB, respectively, which suit the AIA purpose.

In addition, the stability factor of the amplifier can be illustrated by Rollet’s K -factor [38]:

$$K = \frac{1 - |S_{11}|^2 - |S_{22}|^2 + |\Delta|^2}{2 |S_{12}| |S_{21}|} \quad (1)$$

where S_{11} , S_{12} , S_{21} , and S_{22} are the two-port scattering parameters of the amplifier network and Δ is the determinant of the matrix that consists of the scattering parameters. The condition of stability requires $K > 1$. A similar stability measure is μ test [38], where μ is determined by:

$$\mu = \frac{1 - |S_{11}|^2}{|S_{22} - \Delta S_{11}^*| + |S_{12} S_{21}|} \quad (2)$$

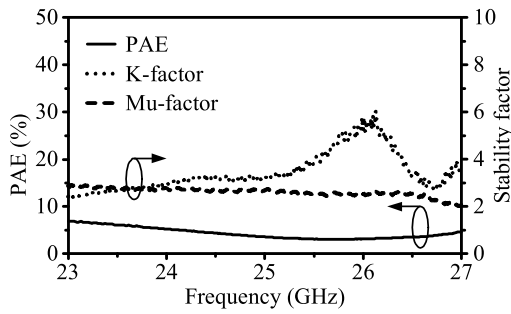


FIGURE 10. Power added efficiency and stability analysis of the power amplifier network.

The unconditional stability requires the μ stability factor to be greater than one. A larger magnitude of μ indicates a more stable amplifier network. The results of the two stability tests are shown in Figure 10. The measured K and μ factors at 25.0 GHz are 3.3 and 2.7, respectively, which indicate that the amplifier network is unconditionally stable. We also evaluate the power added efficiency (PAE) and the noise figure. The PAE results are also provided in Figure 10. At 25.0 GHz, the PAE is 4.0%, and the noise figure is 2.5 dB.

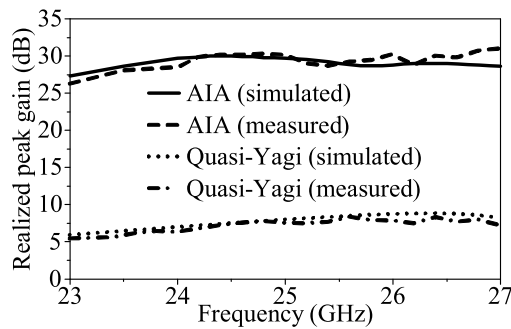


FIGURE 11. Realized peak gain of the AIA and the quasi-Yagi antenna.

Next, the amplifier network and the quasi-Yagi antenna are integrated. Figure 11 is the realized peak gain of the AIA. This realized peak gain evaluates the overall maximum gain and the impedance matching of the input port. The simulated and measured realized peak gain at 25.0 GHz are 29.7 dB and 30.3 dB, respectively, which are almost identical. As a comparison, Figure 11 also provides the realized peak gain of the quasi-Yagi antenna alone, and the simulated and measured antenna gain are 8.0 dBi and 7.6 dBi, respectively. The difference of the gain is about 20 dB, which is attained by the transducer power gain of the amplifier network. More explicitly, Figure 12 is the antenna gain patterns of the AIA and the quasi-Yagi antenna. Good agreement can be found between the simulated and measured patterns. Both the E-plane and H-plane patterns depict gain enhancement of about 20 dB. Accordingly, we arrange the AIA module as the feeding antenna.

B. OPTICALLY TRANSPARENT REFLECTARRAY

The design goal of the reflectarray module is to optimize the geometry for synthesizing required reflection

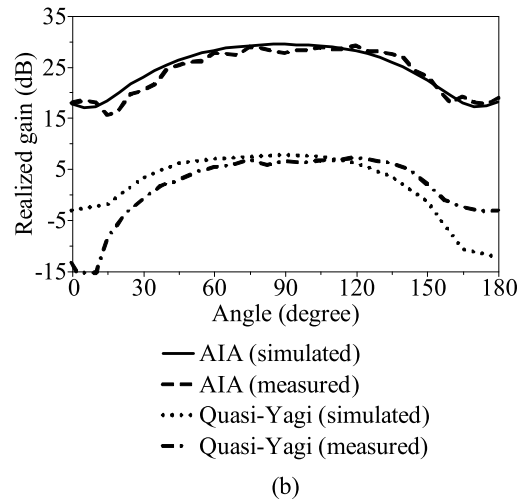
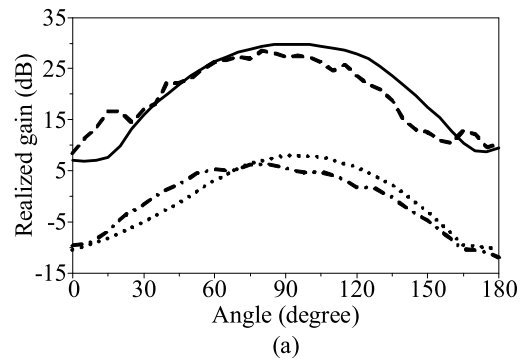


FIGURE 12. Gain patterns of the AIA and the quasi-Yagi antenna. (a) E-plane. (b) H-plane.

phase distributions. First of all, we evaluate the level curves of the reflection phase in terms of the position of elements. The required phase of the i^{th} element, denoted by φ_i , is computed by [39]:

$$\varphi_i = k_0 \times (R_i - \bar{r}_i \cdot \hat{r}_0) \tag{3}$$

where k_0 is the propagation constant in free space, R_i is the separation from the phase center of the AIA to the i^{th} element, \bar{r}_i is the vector from the center of the reflectarray to the i^{th} element, and \hat{r}_0 is the unit vector in the main beam direction. In this study, \hat{r}_0 is selected as the broadside direction.

Figure 13 is the result of the required phase distributions. To realize the phase shifts, the unit cell should be able to provide a phase range of full 360° . In addition, the unit cell is required to demonstrate low additional loss and low design sensitivity. The design sensitivity is defined by the slope of the phase over a $1-\mu\text{m}$ variation of geometric parameters. Moreover, stacking multiple layers reduces transparency as well as the output power of the solar cells, so our application is more suitable to single-layer unit cell designs despite the decreased phase range.

Accordingly, we analyze the phase range, loss, and design sensitivity of 15 single-layer unit cells, including a rectangular patch, circular patch, patch etched with a slot, square ring, dual square ring, circular ring, dual circular ring, double-split ring, cross ring, two types of Jerusalem cross, ring cross,

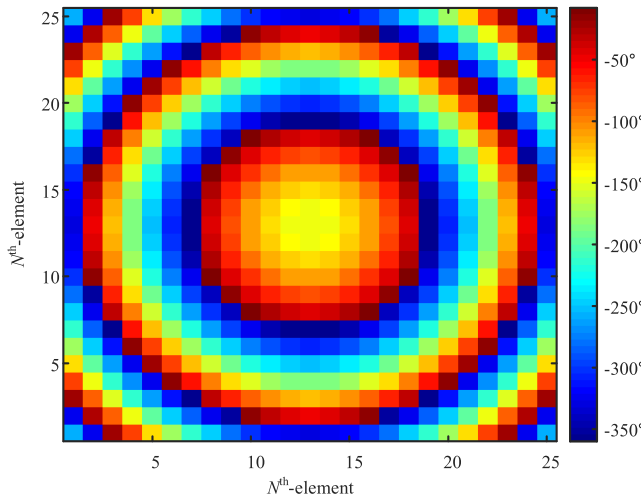


FIGURE 13. Phase distributions of the reflectarray.

square ring with a patch, circular ring with a patch, and spiral. These topologies have been considered as a potential unit cell in the literature. They are designed and optimized to operate at 25.0 GHz, implemented using the material properties described in Section II-B.

Figure 14 is the characteristics of these unit cells. These results are obtained by conducting full-wave HFSS simulation. Some topologies exhibit a phase range of 360°, but the loss is greater than 7 dB (the ring cross, square ring with a patch, circular ring with a patch, and spiral). The unit cell with the lowest additional loss is the rectangular patch. The associated phase range is 295°, and the design sensitivity is the third lowest over these topologies. Only the patch etched with a slot and the square ring show lower sensitivity, whereas the loss is greater than 3.7 dB. Thus, we design the full transparent reflectarray using the rectangular patch, removing the elements whose required phase is beyond 295°.

Next, the dimensions of the reflectarray and the associated number of unit cells are determined by the sensitivity of the overall gain. We arrange the quasi-Yagi antenna as the feed, optimizing reflectarray designs for different numbers of unit cells. In particular, reflectarrays with 1 × 1, 3 × 3, 5 × 5, ..., 25 × 25, and 27 × 27 unit cells are developed. Figure 15 shows the resultant directivity as the function of the number of elements. The results are evaluated by conducting full-wave simulation. In general, the more number of the elements, the higher the directivity is. However, the increase of directivity depicts a trend toward convergence, which is caused by a reduced effective aperture. When the number of unit cells is greater than 25 × 25, aperture efficiency decreases significantly, and the outer unit cells provide incremental improvements. Thus, the case of 423 elements is implemented.

As the dimensions of the aperture are determined, the optimal focal distance can be estimated based on the largest spillover efficiency (denoted by η_s) multiplied by the illumination efficiency (denoted by η_i) [40]. The spillover

No.	Structure	Topology	Phase range (degree)	Loss (dB)	Sensitivity (degree / μm)
1	Rectangular patch		295	1.79	0.36
2	Circular patch		293	2.23	0.44
3	Patch etched with a slot		219	3.73	0.26
4	Square ring		321	6.72	0.26
5	Dual square ring		342	13.92	1.54
6	Circular ring		320	5.81	0.79
7	Dual circular ring		296	5.86	0.69
8	Double-splitting ring		142	12.94	1.55
9	Cross		258	3.30	0.25
10	Jerusalem cross 1		295	6.86	0.52
11	Jerusalem cross 2		184	4.19	0.40
12	Ring cross		362	7.14	0.57
13	Square ring with a patch		359	20.39	0.52
14	Circular ring with a patch		479	11.66	4.25
15	Spiral		666	21.24	8.77

FIGURE 14. Characteristics of the unit cell with various topologies.

efficiency, η_s , is computed by:

$$\eta_s = 1 - \cos^{2q+1}\theta \tag{4}$$

where $\cos^q\theta$ is the fitted normalized pattern of the feed and θ is the observational angle. The spillover efficiency is the function of the ratio between the focal distance (denoted by F) and the maximum dimension of the reflectarray (denoted by D). As shown in Figure 12, the feeding quasi-Yagi antenna has different E-plane and H-plane patterns, which can be fitted using $q = 5.2$ and $q = 2.0$, respectively.

On the other hand, the illumination efficiency, η_i , is determined by:

$$\eta_i = \frac{\left(\frac{1 - \cos^{q+1}\theta}{q+1} + \frac{1 - \cos^q\theta}{q}\right)^2}{2 \tan^2\theta \left(\frac{1 - \cos^{2q+1}\theta}{2q+1}\right)} \tag{5}$$












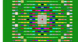


No.	Number of elements	Topology	Directivity (dBi)	Increase of directivity (dB)
1	1		10.9	—
2	9		11.3	0.47
3	25		11.45	0.12
4	49		11.2	-0.26
5	81		14.4	3.23
6	121		17.6	3.22
7	165		19.3	1.66
8	213		20.2	0.9
9	261		21.4	1.2
10	321		22.8	1.4
11	355		23.5	0.65
12	389		23.9	0.46
13	423		24.4	0.5
14	455		24.7	0.3

FIGURE 15. Gain enhancement as the function of the number of elements.

The illumination efficiency is also affected by F/D . Accordingly, η_s , η_i , and the total efficiency ($\eta_s \times \eta_i$) can be computed for various focal distances. Figure 16 is the results of the three types of efficiency. The F/D that leads to the largest total efficiency on the E-plane and H-plane are 0.80 and 0.55, respectively. To balance the tradeoff, the focal distance is selected as $0.68 \times D$, namely, 80.2 mm.

Finally, the optimal transparent reflectarray is constructed. Figure 17 exhibits the fabricated prototype of the proposed reflectarray. By using the feeding quasi-Yagi antenna, the radiation features are measured in an anechoic chamber. Figure 18 is the simulated and measured realized peak gain. The simulated and measured results at 25.0 GHz are 21.5 dBi and 21.4 dBi, respectively. Figure 18 also provides antenna efficiency. The simulated and measured antenna efficiency at 25.0 GHz are 66.6% and 62.9%, respectively. Considering the loss of ITO and soda-lime glass, the efficiency is acceptable.

Moreover, Figure 19 presents the simulated and measured realized gain patterns. The main beam is pointed at

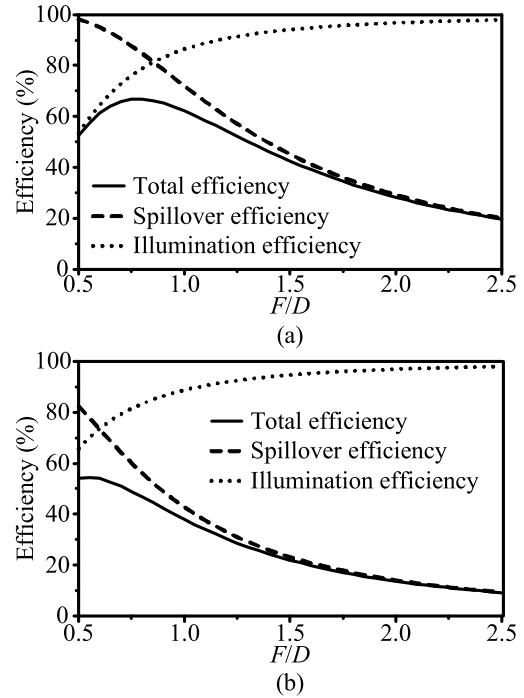


FIGURE 16. Spillover efficiency, illumination efficiency and their product for the transparent reflectarray. (a) E-plane. (b) H-plane.

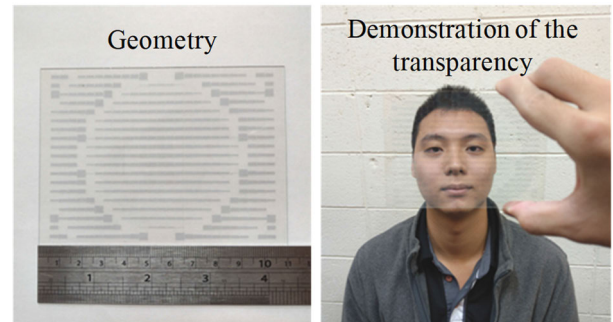


FIGURE 17. Photographs of the optically transparent reflectarray.

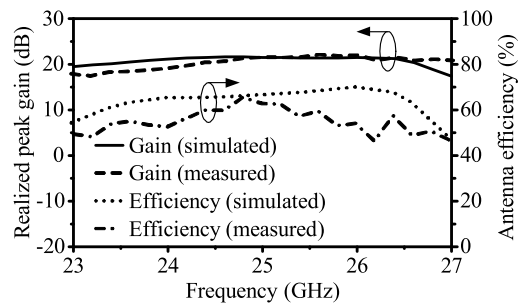


FIGURE 18. Realized peak gain and antenna efficiency of the transparent reflectarray fed by the quasi-Yagi antenna.

the broadside direction. The measured half-power beam widths (HPBWs) in the E-plane and H-plane are 11° and 9° , respectively. The sidelobe levels for the both cuts are greater than 20 dB. These radiation performances are promising for the transparent reflectarray fabricated using ITO and glass.

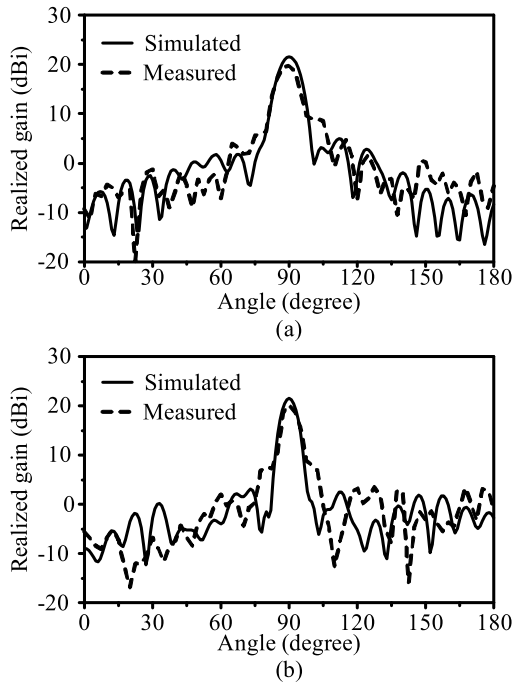


FIGURE 19. Gain patterns of the transparent reflectarray fed by the quasi-Yagi antenna. (a) E-plane. (b) H-plane.

C. POWER MANAGEMENT MODULE

At this stage, the AIA and reflectarray modules have been examined. The investigation is shifted to the third module. The goal of the power management module is to supply sufficient input power to the PA and the sensor. This relies on examining the transparency of the reflectarray prototype and validating the operation of the onboard electronic.

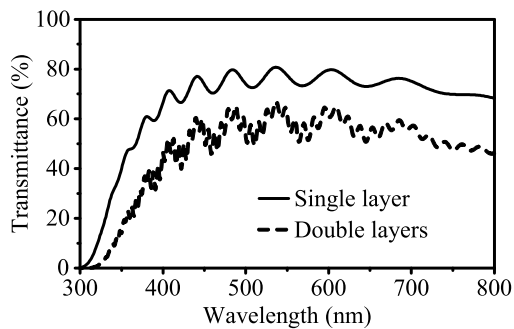


FIGURE 20. Test of transparency for the ITO and soda-lime glass.

Figure 20 shows the transmittance of the reflectarray over the visible EM spectrum (400–800 nm). The measurement is performed with a UV-visible spectrometer S-3100 from Scinco, Taiwan. The results are evaluated for light traveling at normal incidence from the free space through the ITO and glass layers. For the single-layer structure, the transmittance varies from 67.6% to 80.8% over the visible spectrum, and the average transparency is 73.9%. In contrast, for the double-layer structure, the transmittance is between 41.7% and 67.0%, and the average transparency is 54.6%. As expected, stacking two layers results in decreased transparency. However, as the manufacture cost of double-sided

coating is significantly higher than that of one-sided coating, we implement the reflectarray as two stacked layers, instead of one layer of glass with two-sided coating.

To validate the effectiveness of the output power, we attach a solar panel whose dimensions are the same as the optically transparent reflectarray (110 × 80 mm²). When the entire structure is put under exposure to natural daylight, the output voltage, current, and power are 6.8 V, 150 mA, and 1020 mW, respectively. Such power is significantly higher than the required power for biasing the PA (157.5 mW), and the rest of the power is also greater than the driving power of the sensor DHT11 (13.75 mW). Accordingly, the amount of harvested energy is not significantly degraded by the presence of the proposed antenna sub-system even though the double-layer design is implemented.

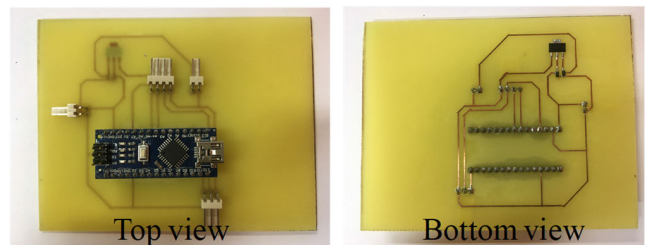


FIGURE 21. Photographs of the power management module.

Figure 21 is the fabricated prototype of the power management module. By connecting the proposed scheme to the solar panel, the output voltage biasing the AIA is regulated as 3.5 V, which further activates the amplifier. Meanwhile, the remaining power successfully drives the sensor.

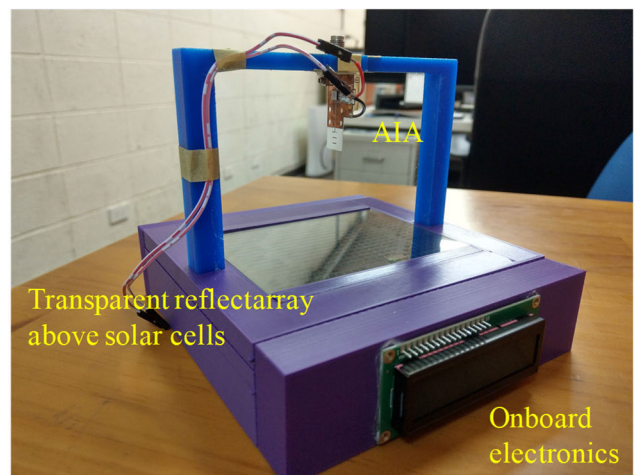


FIGURE 22. Photograph of the proposed antenna prototype.

D. OVERALL PERFORMANCE

Finally, the three modules are integrated, and they construct a full antenna sub-system for CubeSats. Figure 22 shows the integrated prototype of the proposed antenna sub-system. By employing 3-D printing technology, a special fixture is fabricated, and it houses the three modules as well as

the sensor. Although the dc wires that bias the PA are embedded in the 3D-printing fixture, Figure 22 demonstrates the wires as external wiring for clarifying the connection manner. When this system is placed under exposure to light sources, the LCD on the side will exhibit humidity and temperature information, validating that the harvested energy is sufficient. Meanwhile, the AIA module is activated, and the antenna performances can be measured.

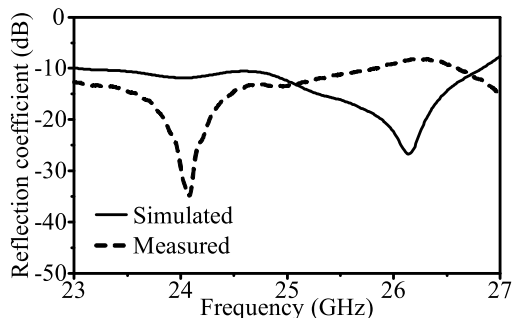


FIGURE 23. Reflection coefficients of the proposed antenna sub-system.

Figure 23 exhibits the input reflection coefficients of the full antenna sub-system. The input port is defined across the SMA connector mounted to the AIA. Although a frequency shift is observed, the simulated and measured reflection coefficients at 25.0 GHz are -12.4 dB and -13.4 dB, respectively, demonstrating that 94.2% and 95.4% of the input power are collected by the antenna. Additional studies are performed to analyze the mismatch between simulated and measured results. When the dielectric constant is set to $\epsilon_r = 3.68$, the resonant frequency shifts to a lower value. In addition, as the prototype of the overall antenna system requires a 3D-printing fixture ($\epsilon_r = 3.5$), which is modelled as free space ($\epsilon_r = 1$) in the full-wave simulation, this causes disagreement between simulation and measurement. These observations indicate that the dielectric constant of the substrate used is higher than the nominal value, and the assembly process introduces experimental errors.

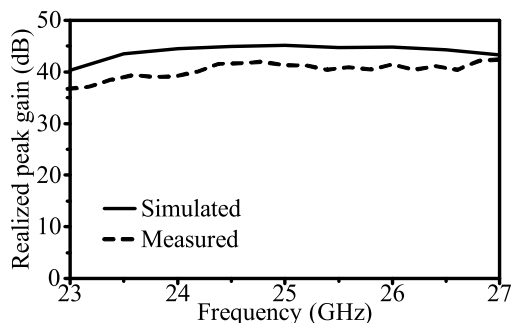


FIGURE 24. Realized peak gain of the proposed antenna sub-system.

Figure 24 depicts the realized peak gain. The simulated and measured realized gain at 25.0 GHz are 45.1 dB and 41.3 dB, respectively. By combining the two gain-enhancement approaches, namely, the AIA and reflectarray, the gain soars up even though the design space is limited to

110×80 mm². It is noted that this design space does not require a clearance area. As solar panels are already setup on the surface of CubeSats, the optically transparent reflectarray can be placed on top of these solar panels directly.

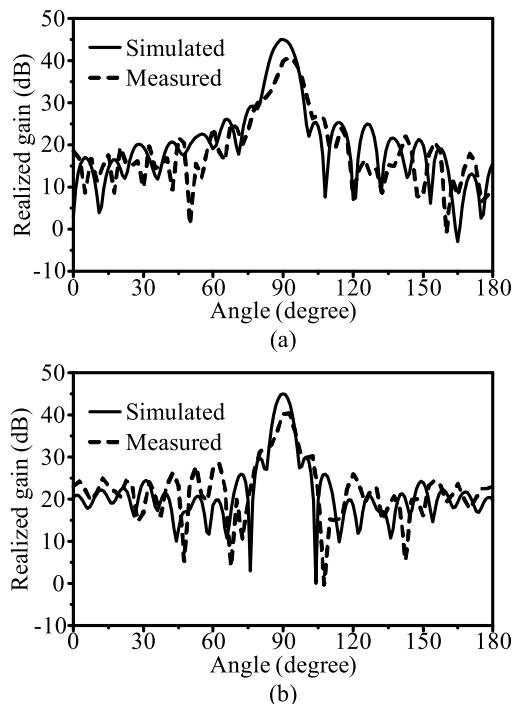


FIGURE 25. Gain patterns of the proposed antenna sub-system. (a) E-plane. (b) H-plane.

Figure 25 is the radiation patterns in terms of realized gain. The trends of the simulated and measured results agree well. The main beam of the full antenna sub-system is still directed to the broadside. These results indicate that the desired directional property with enhanced gain can be achieved using the proposed antenna sub-system.

IV. DISCUSSIONS

The comparison of measured realized peak gain with previous CubeSat antennas is shown in Table 1. In fact, it is not very fair to compare the gain straightforwardly, as these antennas are designed with different frequencies and footprints. However, the gain enhancement of the proposed scheme is still noticeable; the dimensions of the proposed reflectarray are 110×80 mm², whereas the gain is comparable with the reflector with a diameter of 500 mm at 35.75 GHz [4]. The gain is 10 times higher than the reflector with a diameter of 713 mm at X band [3]. Our future work is to implement the proposed scheme in S-band CubeSats. The current reflectarray will be replaced by a miniaturized transparent metasurface [41] on solar cells. Along with a solar-powered AIA, the gain can be greatly enhanced even in S band.

The comparison of the proposed scheme with the literature concerning optically transparent reflectarrays is shown in Table 2. Thanks to the feeding AIA, the proposed technique exhibits the highest measured peak gain. Even though the feeding AIA is replaced by the quasi-Yagi antenna alone,

the measured realized peak gain is still as high as 21.4 dBi. This result is comparable to the performance in the literature using similar dimensions, as some studies select a 12-dBi horn antenna as the feed. This further suggests the effectiveness of the proposed transparent reflectarray design.

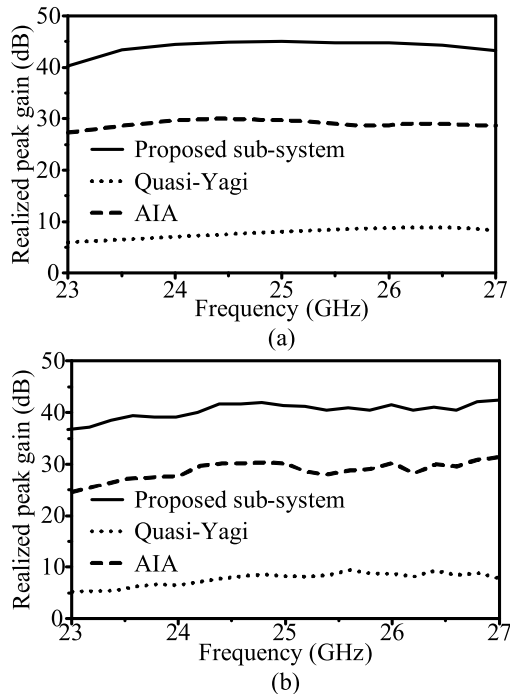


FIGURE 26. Comparison of the gain enhancement. (a) Simulated. (b) Measured.

These performance comparisons validate the significant improvement of gain over compact design space. Such a distinctive feature is obtained by double mechanisms. Figure 26 is the gain comparison for the three designs, including the quasi-Yagi antenna, the AIA, and the finalized antenna sub-system. When the PA is integrated to the quasi-Yagi antenna, the simulated and measured gain improvements at 25.0 GHz are 21.7 dB and 22.7 dB, respectively. Furthermore, when the AIA is implemented as the feed illuminating the transparent reflectarray, the simulated and measured gain improvements at the same frequency are 15.4 dB and 11.0 dB, respectively. Such double mechanisms enable the proposed antenna to demonstrate significant gain enhancement.

The antenna subsystem demonstrated in this paper is a proof-of-concept prototype. The three modules can be implemented by other designs. For example, the PA-type AIA can be constructed using a deployable helical antenna connected with a PA chipset, and the reflectarray module can be fabricated using crystalline n-Si microwires. By integrating the three modules, gain enhancements are noticeable as compared to the earlier designs [3]–[22].

On the other hand, although the proposed design provides promising results, this prototype is not without limitations. In particular, the blockage introduced by the AIA reduces the amount of harvested solar energy. To mitigate the effect of

the blockage, this study employs a feeding antenna with an end-fire radiation pattern, instead of a broadside pattern. Our future work is to implement a reflectarray excited with an offset feed, which can mitigate the adverse effect of feeding blockage more significantly. Another limitation is the lack of feed deployment mechanism. Earlier studies have shown how to pop out the feed of a reflectarray or reflector [2], [6], so this work puts the emphasis on the novel double mechanisms for the gain enhancement. In addition, the transparent reflectarray covers the solar cells directly, without the integration using special materials such as amorphous silicon cells [42] and multilayer structures [31]. If these techniques are employed, the harvested solar energy can be further increased due to maximum optical transmittance.

V. CONCLUSION

In this paper, a new antenna sub-system with enhanced gain and compact size is proposed for CubeSat applications. The implementation and performance have been discussed in detail. By integrating the AIA module, transparent reflectarray module, and power management module, the measured realized peak gain is as high as 41.3 dB at 25.0 GHz, whereas the reflectarray dimensions are only $110 \times 80 \text{ mm}^2$. The distinctive characteristics of the proposed antenna are threefold. First of all, the gain improvements are achieved by double mechanisms; the cascaded PA provides gain enhancement of 22.7 dB, and the transparent reflectarray further raises the gain by 11.0 dB. Second, the AIA module exploits the environmental feature of the space, achieving a sustainable high-gain characteristic by biasing the PA through inexhaustible solar energy. Third, as the transparent reflectarray module is integrated to already existing solar panels, this gain-enhancement scheme does not require an extra clearance area, leading to a very compact footprint. To the best of our knowledge, the three features have not yet been presented and integrated for CubeSat applications. The proposed scheme is expected to provide performance improvements for future satellite antenna development.

REFERENCES

- [1] Y. Rahmat-Samii and A. C. Densmore, "Technology trends and challenges of antennas for satellite communication systems," *IEEE Trans. Antennas Propag.*, vol. 63, no. 4, pp. 1191–1204, Apr. 2015.
- [2] S. Gao, Y. Rahmat-Samii, R. E. Hodges, and X.-X. Yang, "Advanced antennas for small satellites," *Proc. IEEE*, vol. 106, no. 3, pp. 391–403, Mar. 2018.
- [3] A. Babuscia, J. Sauder, A. Chandra, J. Thangavelautham, L. Feruglio, and N. Bienert, "Inflatable antenna for CubeSat: A new spherical design for increased X-band gain," in *Proc. IEEE Aerosp. Conf.*, Big Sky, MT, USA, Mar. 2017, pp. 1–10.
- [4] N. Chahat, R. E. Hodges, J. Sauder, M. Thomson, E. Peral, and Y. Rahmat-Samii, "CubeSat deployable ka-band mesh reflector antenna development for Earth science missions," *IEEE Trans. Antennas Propag.*, vol. 64, no. 6, pp. 2083–2093, Jun. 2016.
- [5] M. McNicholas, J. Deluna, R. Manno, and Y.-H. Shu, "Low cost ka-band transmitter for CubeSat systems," in *Proc. Topical Workshop Internet Space (TWIOS)*, Phoenix, AZ, USA, Jan. 2017, pp. 1–4.
- [6] R. E. Hodges, N. Chahat, D. J. Hoppe, and J. D. Vacchione, "A deployable high-gain antenna bound for Mars: Developing a new folded-panel reflectarray for the first CubeSat mission to Mars," *IEEE Antennas Propag. Mag.*, vol. 59, no. 2, pp. 39–49, Apr. 2017.

- [7] C. J. Vourch and T. D. Drysdale, "V-band 'bull's eye' antenna for CubeSat applications," *IEEE Antennas Wireless Propag. Lett.*, vol. 13, pp. 1092–1095, 2014.
- [8] J. Padilla, G. Rosati, A. Ivanov, F. Bongard, S. Vaccaro, and J. Mosig, "Multi-functional miniaturized slot antenna system for small satellites," in *Proc. Eur. Conf. Antennas Propag. (EuCAP)*, Rome, Italy, May 2011, pp. 2170–2174.
- [9] A. J. Ernest, Y. Tawk, J. Costantine, and C. G. Christodoulou, "A bottom fed deployable conical log spiral antenna design for CubeSat," *IEEE Trans. Antennas Propag.*, vol. 63, no. 1, pp. 41–47, Jan. 2015.
- [10] J. Costantine, Y. Tawk, I. Maqueda, M. Sakovsky, G. Olson, S. Pellegrino, and C. G. Christodoulou, "UHF deployable helical antennas for CubeSats," *IEEE Trans. Antennas Propag.*, vol. 64, no. 9, pp. 3752–3759, Sep. 2016.
- [11] T. Yasin and R. Baktur, "Circularly polarized meshed patch antenna for small satellite application," *IEEE Antennas Wireless Propag. Lett.*, vol. 12, pp. 1057–1060, Aug. 2013.
- [12] M. T. Islam, M. Cho, M. Samsuzzaman, and S. Kibria, "Compact antenna for small satellite applications," *IEEE Antennas Propag. Mag.*, vol. 57, no. 2, pp. 30–36, Apr. 2015.
- [13] E. Armeri, L. Boccia, G. Amendola, and G. Di Massa, "A compact high gain antenna for small satellite applications," *IEEE Trans. Antennas Propag.*, vol. 55, no. 2, pp. 277–282, Feb. 2007.
- [14] J. Li, S. Gao, and J. Xu, "Circularly polarized high-gain printed antennas for small satellite applications," in *Proc. Int. Conf. Microw. Technol. Comput. Electromagn. (ICMTC)*, Beijing, China, Nov. 2009, pp. 76–79.
- [15] Y. Yao, S. Liao, J. Wang, K. Xue, E. A. Balfour, and Y. Luo, "A new patch antenna designed for CubeSat: Dual feed, L/S dual-band stacked, and circularly polarized," *IEEE Antennas Propag. Mag.*, vol. 58, no. 3, pp. 16–21, Jun. 2016.
- [16] F. E. Tubbal, R. Raad, K.-W. Chin, and B. Butters, "S-band shorted patch antenna for inter pico satellite communications," in *Proc. 8th Int. Conf. Telecommun. Syst. Services Appl. (TSSA)*, Kuta, India, Oct. 2014, pp. 1–4.
- [17] E. Pittella, S. Pisa, M. Pontani, A. Nascetti, P. D'Atanasio, A. Zambotti, and H. Hadi, "Reconfigurable S-band patch antenna system for cubesat satellites," *IEEE Aerosp. Electron. Syst. Mag.*, vol. 31, no. 5, pp. 6–13, May 2016.
- [18] A. Nascetti, E. Pittella, P. Teofilatto, and S. Pisa, "High-gain S-band patch antenna system for Earth-observation CubeSat satellites," *IEEE Antennas Wireless Propag. Lett.*, vol. 14, pp. 434–437, Nov. 2015.
- [19] T. K. Sreeja, A. Arun, and J. J. Kumari, "An S-Band micro-strip patch array antenna for nano-satellite applications," in *Proc. Int. Conf. Green Technol. (ICGT)*, Trivandrum, India, Dec. 2012, pp. 325–328.
- [20] F. Qin, S. Gao, G. Wei, Q. Luo, C. Mao, C. Gu, J. Xu, and J. Li, "Wideband circularly polarized Fabry-Pérot antenna [antenna applications corner]," *IEEE Antennas Propag. Mag.*, vol. 57, no. 5, pp. 127–135, Oct. 2015.
- [21] G. F. Kurnia, B. S. Nugroho, and A. D. Prasetyo, "Planar inverted-F antenna (PIFA) array with circular polarization for nano satellite application," in *Proc. Int. Symp. Antennas Propag. (ISAP)*, Kaohsiung, Taiwan, Dec. 2014, pp. 431–432.
- [22] S. Gunaseelan and M. Murugan, "High gain patch antenna for CubeSat," in *Proc. Int. Conf. Wireless Commun., Signal Process. Netw. (WiSPNET)*, Chennai, India, Mar. 2016, pp. 52–54.
- [23] W. R. Deal, V. Radisic, Y. Qian, and T. Itoh, "Integrated-antenna push-pull power amplifiers," *IEEE Trans. Microw. Theory Techn.*, vol. 47, no. 8, pp. 1418–1425, Aug. 1999.
- [24] C. Y. Hang, W. R. Deal, Y. Qian, and T. Itoh, "High-efficiency push-pull power amplifier integrated with quasi-Yagi antenna," *IEEE Trans. Microw. Theory Techn.*, vol. 49, no. 6, pp. 1155–1161, Jun. 2001.
- [25] S. K. Dhar, O. Hammi, M. S. Sharawi, and F. M. Ghannouchi, "Power amplifier based integrated and miniaturized active antenna," in *Proc. 9th Eur. Conf. Antennas Propag. (EuCAP)*, Lisbon, Portugal, Apr. 2015, pp. 1–4.
- [26] C. Kocia and S. V. Hum, "Design of an optically transparent reflectarray for solar applications using indium tin oxide," *IEEE Trans. Antennas Propag.*, vol. 64, no. 7, pp. 2884–2893, Jul. 2016.
- [27] T. Yekan, R. Baktur, C. Swenson, O. Kegege, S. Altunc, H. Shaw, J. Lyons, and M. Deshpande, "Transparent reflectarray antenna printed on solar cells," in *Proc. IEEE 43rd Photovoltaic Specialists Conf. (PVSC)*, Portland, OR, USA, Jun. 2016, pp. 2610–2612.
- [28] T. Yekan and R. Baktur, "Design of two transparent X band reflectarray antennas integrated on a satellite panel," in *Proc. IEEE Int. Symp. Antennas Propag. (APSURSI)*, Fajardo, Puerto Rico, Jun. 2016, pp. 1413–1414.
- [29] M. A. Moharram and A. A. Kishk, "Optically transparent reflectarray antenna design integrated with solar cells," *IEEE Trans. Antennas Propag.*, vol. 64, no. 5, pp. 1700–1712, May 2016.
- [30] M. A. Moharram and A. A. Kishk, "A ka band optically transparent reflectarray design integrated with solar cells," in *Proc. IEEE Int. Conf. Ubiquitous Wireless Broadband (ICUWB)*, Montreal, QC, Canada, Oct. 2015, pp. 1–4.
- [31] W. An, L. Xiong, S. Xu, F. Yang, H.-P. Fu, and J.-G. Ma, "A ka-band high-efficiency transparent reflectarray antenna integrated with solar cells," *IEEE Access*, vol. 6, pp. 60843–60851, Oct. 2018.
- [32] S. H. Zainud-Deen, W. M. Hassan, and H. A. Malhat, "B1. Investigation into the effects of solar cells on the DRA reflectarray/transmitarray antenna design," in *Proc. 32nd Nat. Radio Sci. Conf. (NRSC)*, 6th of October City, Egypt, Mar. 2015, pp. 1–8.
- [33] C. Kocia and S. V. Hum, "Optically transparent reflectarray for satellite applications," in *Proc. 8th Eur. Conf. Antennas Propag. (EuCAP)*, The Hague, The Netherlands, Apr. 2014, pp. 1607–1610.
- [34] T. Yekan and R. Baktur, "Conformal integrated solar panel antennas: Two effective integration methods of antennas with solar cells," *IEEE Antennas Propag. Mag.*, vol. 59, no. 2, pp. 69–78, Apr. 2017.
- [35] Z.-W. Miao, Z.-C. Hao, Y. Wang, B.-B. Jin, J.-B. Wu, and W. Hong, "A 400-GHz high-gain quartz-based single layered folded reflectarray antenna for terahertz applications," *IEEE Trans. THz Sci. Technol.*, vol. 9, no. 1, pp. 78–88, Jan. 2019.
- [36] H. K. Kan, R. B. Waterhouse, A. M. Abbosh, and M. E. Bialkowski, "Simple broadband planar CPW-fed quasi-Yagi antenna," *IEEE Antennas Wireless Propag. Lett.*, vol. 6, pp. 18–20, 2007.
- [37] Analog Devices, Norwood, MA, USA. [Online]. Available: <https://www.analog.com>
- [38] D. M. Pozar, *Microwave Engineering*, 3rd ed. New York, NY, USA: Wiley, 2005.
- [39] D. M. Pozar, S. D. Targonski, and H. D. Syrigos, "Design of millimeter wave microstrip reflectarrays," *IEEE Trans. Antennas Propag.*, vol. 45, no. 2, pp. 287–295, Feb. 1997.
- [40] M. Zebrowski, "Illumination and spillover efficiency calculations for rectangular reflectarray antennas," *High Freq. Des.*, vol. 1, pp. 28–38 Dec. 2012.
- [41] Y.-S. Chen and T.-Y. Ku, "A low-profile wearable antenna using a miniature high impedance surface for smartwatch applications," *IEEE Antennas Wireless Propag. Lett.*, vol. 15, pp. 1144–1147, 2016.
- [42] A. Rashidian, L. Shafai, and C. Shafai, "Miniaturized transparent met-allo dielectric resonator antennas integrated with amorphous silicon solar cells," *IEEE Trans. Antennas Propag.*, vol. 65, no. 5, pp. 2265–2275, May 2017.



YEN-SHENG CHEN (Member, IEEE) was born in Taichung, Taiwan. He received the B.S. degree in electrical engineering, and the M.S. and Ph.D. degrees in communication engineering from National Taiwan University, Taipei, Taiwan, in 2007, 2009, and 2012, respectively.

Since 2013, he has been a Faculty Member of the Department of Electronics Engineering, National Taipei University of Technology, Taipei, where he is currently a Professor. He has participated in a wide range of research projects, including chipless RF identification, mm-wave antennas and circuits, RF energy harvesting, antenna array failure correction, antennas for body centric communications, microwave reconfigurable components, and multiobjective optimization techniques. His current research interests include chipless sensor networks, high-gain antennas, and antenna theory.

Dr. Chen has been a recipient of the Outstanding Reviewers Award for the IEEE ANTENNAS AND WIRELESS PROPAGATION LETTERS, since 2017, and was a recipient of the Dr. Shechtman Young Researcher Award from the National Taipei University of Technology, in 2018, the Outstanding Reviewers Award for the IEEE TRANSACTIONS ON ANTENNAS AND PROPAGATION, in 2019, the Outstanding Research Award from the College of Electrical Engineering and Computer Science, National Taipei University of Technology, in 2018 and 2019, and the Outstanding Research Award from the National Taipei University of Technology, in 2019. He has served on the editorial/review boards for many technical journals, transactions, proceedings, and letters.



YU-HONG WU was born in Taoyuan, Taiwan. He received the B.S. degree in electro-optical engineering from National Formosa University, Huwei, Taiwan, in 2017, and the M.S. degree in electronics engineering from the National Taipei University of Technology, Taipei, Taiwan, in 2019.

He is currently a Senior RF Engineer with Chunghwa Precision Test Tech. (CHPT) Company Ltd., where he is responsible for signal integrity (SI) and the power integrity (PI) analysis of vertical probe card.



CHIA-CHI CHUNG was born in Tainan, Taiwan. He received the B.S. degree in electronics engineering from the National Yunlin University of Science and Technology, Douliu, Taiwan, in 2018. He is currently pursuing the M.S. degree in electronics engineering with the National Taipei University of Technology, Taipei, Taiwan.

His current research interests include metasurfaces, antennas, and array antenna design.

...